ADVANCING EARTH AND SPACE SCIENCES

Space Weather

RESEARCH ARTICLE
10.1029/2024SW004160

Predicting the SYM-H Index Using the Ring Current Energy Balance Mechanism

Lan Ma[1], Yong Ji[2], Chao Shen[1,3], Gang Zeng[4], Peng E[3], YanYan Yang[5], Shuo Ti[6], and Nisar Ahmad[7]

[1]School of Science, Harbin Institute of Technology (Shenzhen), Shenzhen, China, [2]School of Mathematics and Statistics; Ningxia Key Laboratory of Interdisciplinary Mechanics and Scientific Computing; Ningxia Basic Science Research Center of Mathematics, Ningxia University, Yinchuan, China, [3]National Key Laboratory of Space Environment and Matter Behaviors, Harbin Institute of Technology, Harbin, China, [4]School of Mathematics and Physics, Jingchu University of Technology, Jingmen, China, [5]National Institute of Natural Hazards, Ministry of Emergency Management of China, Beijing, China, [6]State Key Laboratory of Space Weather, National Space Science Center, Chinese Academy of Sciences, Beijing, China, [7]Department of Physics, Qilu Institute of Technology, Jinan, P. R. China

Key Points:

- The balance mechanism of ring current particles' kinetic energy is used to construct algorithm predicting SYM-H
- The formula of energy coupling function for ring current is determined
- The lifetime of ring current particles during quiet and storm period is identified based on neural network

Correspondence to:

C. Shen and Y. Ji,
shenchao@hit.edu.cn;
jiyong@nxu.edu.cn

Citation:

Ma, L., Ji, Y., Shen, C., Zeng, G., E, P., Yang, Y., et al. (2025). Predicting the SYM-H index using the ring current energy balance mechanism. *Space Weather*, *23*, e2024SW004160. https://doi.org/10.1029/2024SW004160

Received 12 SEP 2024
Accepted 16 FEB 2025

Author Contributions:

Conceptualization: Lan Ma, Yong Ji
Data curation: Lan Ma, Peng E
Formal analysis: Lan Ma, Yong Ji
Funding acquisition: Chao Shen, Peng E
Investigation: Lan Ma
Methodology: Lan Ma, Yong Ji
Project administration: Chao Shen
Resources: Lan Ma
Software: Yong Ji
Supervision: Yong Ji, Chao Shen, Peng E
Validation: Lan Ma
Visualization: Lan Ma
Writing – original draft: Lan Ma
Writing – review & editing: Yong Ji, Chao Shen, Gang Zeng, Peng E, YanYan Yang, Shuo Ti, Nisar Ahmad

Abstract

The geomagnetic disturbance index SYM-H is primarily determined by the total kinetic energy of ring current particles. Therefore, the energy balance mechanism of the ring current can be used to construct an SYM-H evolution equation for prediction purposes. This study extends a modeling concept developed by Ji et al. (2023), https://doi.org/10.1029/2022ea002560 to establish an algebraic equation for predicting the SYM-H index based on equilibrium between energy injection and ring current loss. The loss term in the model is determined by a fully connected neural network. The fundamental form of the energy injection function is derived from existing solar wind–magnetosphere energy coupling functions, with its scale factor adjusted as a free-fitting parameter to optimize the prediction of observations. After being trained on solar wind and SYM-H observations from 20 magnetic storms, the new model predicts the SYM-H index well 1 hr and 2 hr in advance, with root mean square errors of 6.7 and 8.9 nT, respectively. These accuracies represent a 7% (1-hr model) and a 6% (2-hr model) improvement over the previous model. Furthermore, the scale factors for the solar wind parameters in the energy coupling function determined by the new model can be explained by the previous observations in the magnetic tail current sheet, confirming that the ring current energy primarily originates from the current sheet. The lifetime of the ring current particles, as determined by the neural network, varies with the SYM-H index. It is approximately 6 hr for the fast recovery phase and more than 10 hr for the slow recovery phase, consistent with the dominant ring current particles changing from oxygen ions to protons during intense storms.

Plain Language Summary

The energy and matter carried by the solar wind can enter the Earth's magnetosphere and induce disturbances of magnetic field near the earth. The SYM-H index is constructed to quantify the intensity of these disturbances which is positively correlated with space weather disaster events. Therefore, predicting the SYM-H index is of significance for space mission. This study further optimizes the algorithm for predicting the SYM-H index based on the total kinetic energy balance mechanism of ring current and proposes a new model. The new model constructs the energy injection function of the ring current based on an empirical solar wind-magnetosphere energy coupling function. Neural networks are used to characterize the loss process of the ring current, successfully distinguishing the fast and slow recovery phases and identifying ring current particle lifetimes, which are consistent with observations. The prediction accuracy of SYM-H is also comparable to other neural network models, making it applicable for space weather operations and useful for studying the physical mechanisms of solar wind-magnetosphere energy transport.

1. Introduction

The magnetosphere is constantly engaged in complex nonlinear interactions with the solar wind (Baker et al., 2007; Consolini, 2018). Through these interactions, the energy and mass carried by the solar wind can penetrate Earth's inner magnetosphere, leading to significant electromagnetic disturbances. These disturbances increase the flux of energetic particles in the radiation belt, induce current flow in power grids, and trigger space weather events such as satellite surface charging and discharging and power grid failures (Jordanova et al., 2020; Pirjola et al., 2005; Wing et al., 2022). Therefore, understanding the interaction between the solar wind and the magnetosphere is crucial for accurate space weather forecasting. Magnetospheric large-scale convection driven by reconnection is a key mechanism for transporting matter and energy from the solar wind into the magnetosphere, ultimately resulting in magnetic storms and substorms (Nitta et al., 2021) (Y. Q. Yu et al., 2022). When reconnection occurs, the southward interplanetary magnetic field (IMF) reconnects with the Earth's northward magnetic field on the dayside, opening the originally closed magnetopause magnetic field lines. These lines are then advected to the magnetotail, closed again by the reconnection process there, and subsequently transported by the moving plasma to the sunward side, completing the entire convection process (Ahmad et al., 2025; Axford, 1969; Dungey, 1961; Zhang et al., 2015). However, the picture of magnetospheric convection is not singular. Dai et al. (2024) have shown using numerical simulations and observations that even the dayside reconnection process alone can stimulate magnetospheric convection. In addition to convective injection, the solar wind may also penetrate the magnetosphere through the Kelvin–Helmholtz (KH) shear instability or anomalous diffusion at the magnetopause boundary layer (Graham et al., 2022; Hasegawa et al., 2004; Li et al., 2023; Treumann et al., 1991). It has also been shown that wave processes can transfer energy from the solar wind to the ionosphere or inner magnetosphere, where large-scale kinetic and magnetic energy can be converted into thermal energy. In conclusion, solar wind–magnetosphere coupling is a multi-scale and complex process that is difficult to describe accurately with analytical methods. Therefore, the development of an empirical model based on observational data and theory is critical for quantifying the overall impact of the solar wind on the magnetosphere.

Many empirical coupling functions, which are mathematical formulas composed of solar wind parameters such as the velocity, temperature, and magnetic field, have been introduced to characterize the impact of the solar wind on Earth (P. D. Perreault, 1974) (Perreault & Akasofu, 1978; Lockwood, 2022). These coupling functions estimate the energy injection rate from the solar wind into the magnetosphere (Akasofu, 1981; Vasyliunas et al., 1982). Since the system of partial differential equations describing the interaction between the solar wind and the magnetosphere is nonlinear and multifield, it is impossible to solve these equations theoretically and identify a universal coupling function (Finch & Lockwood, 2007; Gonzalez, 1990). However, theoretical considerations can guide researchers toward approximate formulas for the coupling function. For instance, dimensional analysis suggests that energy fluxes carried by the upstream solar wind, such as electromagnetic and mechanical energy flux densities, would be appropriate input functions. This finding leads to a power-law formula for the coupling function that depends on solar wind parameters. The power law also reflects the similarity of multi-scale processes in the magnetosphere (Barenblatt, 1996). It is important to note that the coupling function derived from dimensional analysis includes parameters that are not yet defined. These parameters can be determined by adjusting them to optimize the correlation between geomagnetic disturbances and coupling functions, either using observations of geomagnetic disturbance indices and solar wind data or by calculating the energy input rate from magnetohydrodynamic (MHD) simulation data sets (Bargatze et al., 1985; Borovsky, 2021; Lockwood, 2022). However, MHD simulations may not capture all the details of interactions between the solar wind and the magnetosphere, particularly at smaller scales. Therefore, while MHD data sets are a useful reference, direct observations of the solar wind and geomagnetic indices should also be considered to accurately identify the coupling function.

A portion of the mass and energy from the solar wind that enters the magnetosphere is transported to the ring current, a near-circular flow of charged particles drifting around Earth's dipole field. This ring current primarily consists of hydrogen, oxygen, and electrons from the solar wind and ionosphere (S. Y. Fu et al., 2001). When the IMF is oriented southward, it drives strong large-scale magnetospheric convection, resulting in the injection of particles and energy from the solar wind and ionosphere into the ring current, thereby intensifying it (Daglis, 2006; Ebihara & Ejiri, 2003; Fok et al., 2001). This intensified ring current causes negative disturbances in the magnetic field near the Earth's surface, particularly in equatorial regions. The SYM-H index is used to quantify these disturbances. It represents the average horizontal magnetic field perturbation observed by geomagnetic stations distributed across equatorial regions and longitudes. The SYM-H index has a time resolution of 1 minute, while the Dst index, which is defined similarly, has a time resolution of 1 hr (Mayaud, 1980; Wanliss & Showalter, 2006). According to the Dessler–Parker–Sckopke relation, there is a linear relationship between the intensity of the SYM-H (or Dst) index and the total energy of the ring current. Additionally, because the ring current energy is influenced by interactions between the solar wind and the Earth's magnetosphere, SYM-H can be used as an indicator for evaluating coupling functions. However, it is important to note that SYM-H is also affected by magnetopause currents, magnetotail currents, and ionospheric-induced currents. Therefore, caution is needed when using SYM-H to evaluate coupling functions. Moreover, SYM-H reflects the overall state of the magnetosphere and serves as an input for weather disaster prediction models, such as those forecasting energetic electron flux within the radiation belt (Forsyth et al., 2020; Ganushkina et al., 2017). Consequently, predicting SYM-H indices accurately is of critical importance.

The SYM-H prediction model originated in the work of Burton et al., who derived the time evolution equation for the Dst (SYM-H) index based on the energy balance process of the ring current. In Burton's model, the driving term for Dst is associated with the solar wind input, while the loss term is associated with charge exchange (Burton et al., 1975). When the parameters were calibrated using observed solar wind data from Explorer 33 and 35, Burton's model produced reasonable predictions, stimulating further development of energy balance models (Klimas et al., 1997; McPherron & O'Brien, 2001). These models primarily treat SYM-H evolution as a dynamic system, using either probabilistic optimization techniques or incorporating complex factors to improve the prediction accuracy. Shen et al. (2002) used an auroral electrojet index (AL) as an input parameter to calculate driving electric fields and predict SYM-H values. This model also facilitates a quantitative investigation of the relationship between substorms and magnetic storms. Zhu et al. (2006) applied nonlinear autoregressive moving average model with exogenous inputs (NARMAX) technology to model nonlinear processes in the magnetosphere for Dst predictions and explored the connection between variations in Dst and magnetospheric physical processes. Zhao et al. (2022) used Burton's model to examine SYM-H predictions during intense magnetic storms and found that accuracy decreases with increasing storm intensity. Adjusting for the solar wind dynamic pressure further improved the performance of the Burton model. The key to SYM-H models lies in selecting an appropriate energy injection term, known as the energy coupling function. Burton used the solar wind electric field (Ey) as the coupling function, and subsequent models have explored various alternative forms. New methods must be developed to determine optimal energy coupling functions to achieve more accurate predictions.

Artificial intelligence technologies, such as neural networks, have also been employed to identify correlations between solar wind parameters and SYM-H for prediction purposes (Camporeale, 2019; Pallocchia et al., 2006). This approach relies on large data sets of observations. Since the 1990s, stable and continuous solar wind observations from several spacecraft at the L1 point have validated the use of neural networks for SYM-H predictions. Wu and Lundstedt (1997) used recurrent neural networks (RNNs) to study the interaction between the solar wind and the magnetosphere, determine optimal coupling functions, and propose an RNN model for practical applications. However, during intense magnetic storms, solar wind plasma data is more likely to be incomplete than IMF data due to the limitations of observation instruments. As a result, many prediction models rely primarily on IMF data. Earlier models focused mainly on forecasting the Dst index. Cai et al. (2010) extended the nonlinear autoregressive exogenous model (NARX) neural network to predict SYM-H by using historical SYM-H sequences as network inputs, which improved prediction accuracy, resulting in a root mean square error of 14.2 nT for 1-hr SYM-H predictions. Recently, advancements in computer hardware and the accumulation of observational data have led to significant developments in artificial intelligence technologies, resulting in breakthroughs such as image recognition systems, speech processing algorithms, and interactive language models. These advancements have revitalized progress in space weather forecasting. Deep learning techniques, such as convolutional neural networks and long short-term memory (LSTM) networks, have been successfully applied to SYM-H forecasting, yielding high levels of accuracy (Collado-Villaverde et al., 2021; Siciliano et al., 2021). Iong et al. (2022) developed a SYM-H prediction model with 5-min resolution using gradient boosting machines. Abduallah et al. (2024) introduced SYM-Hnet, which combines graph neural networks with a bidirectional LSTM (BiLSTM) architecture to predict SYM-H using solar wind plasma parameters and IMF values as inputs. This novel model not only provides accurate SYM-H predictions but also incorporates Bayesian statistics to estimate prediction uncertainties. It currently represents the state of the art, achieving an average error of approximately 5 nT. As solar wind observation data continues to accumulate, AI-based models can further improve in accuracy. However, a persistent challenge remains: while data-driven models can predict ordinary magnetic storms accurately, they may become unreliable or deviate significantly during extreme magnetic storms, potentially leading to misjudgments of space weather events.

In summary, the injection of solar wind energy into the magnetospheric system, particularly the ring current, is a complex process that can only be accurately described by a semiempirical model. Traditional models provide clear physics but lack precision, whereas the latest neural network models offer high accuracy but are difficult to interpret and may not guarantee reliable results under extreme conditions. A more effective approach is to design a model based on physical laws while leveraging the powerful fitting capabilities of neural networks to manage complex parameters. Recently, we proposed a composite model that integrates the strengths of Burton's model and neural networks to achieve high-precision SYM-H predictions and explore related physical laws (Ji et al., 2023). However, this composite model uses only the solar wind electric field as its coupling function, which does not fully characterize the energy injection from the solar wind. Therefore, this paper aims to develop an improved model grounded in physical laws by incorporating alternative energy coupling functions and neural network technology. Section 2 presents the algorithm architecture for predicting SYM-H. The accuracy of new predictions and comparison with previous studies are shown in Section 3. Section 4 presents discussions about the formula of coupling function determined by new model, loss process of ring current and the sources of errors of predictions. Finally, conclusions are outlined.

2. Method

The key to the composite model is to consider the relevant physical processes needed to construct a high-accuracy SYM-H prediction model. According to the principle of the Burton et al. model (referred to as the BMR model here), SYM-H primarily results from the contributions of the ring current and the magnetopause current. Since the strength of the magnetopause current is determined by the solar wind dynamic pressure, we define SYM-H* = SYM-H$-bP_S^{(1/2)}$ to specifically represent the contribution from the ring current, where $P_S^{(1/2)}$ denotes the solar wind dynamic pressure. The magnitude of this contribution is positively correlated with the total energy of the ring current. The total energy of the ring current is mainly influenced by injection and loss processes. Magnetospheric convection electric fields determine the amount of energy injected, while loss processes are governed by charge exchange, magnetopause drift, atmospheric precipitation, and Coulomb collisions. The BMR model suggests that convection electric fields are directly related to the solar wind electric field and uses $B_Z V_X$ as an energy injection function. Additionally, the model treats the charge exchange time as the lifetime of the ring current particles and includes a derived time evolution equation for the Dst index. Due to limited observational data, parameters in the BMR model are calibrated in a simplified manner, yet it still provides acceptable predictions. The composite model optimizes the BMR model in two main ways: first, the coefficients in the model are no longer treated as simplified constants or linear functions but are instead determined by neural networks; second, the loss term is separated into charge exchange loss and magnetopause drift loss. This optimization begins with physical considerations. The interaction between the solar wind and the magnetosphere is nonlinear, and the magnetosphere is not merely passively driven by the solar wind. Changes in the state of the magnetosphere also impact the transport of energy and matter from the solar wind. Additionally, charge exchange loss and magnetopause drift loss are distinct mechanisms with difficult-to-distinguish lifetimes. After training with data from 20 magnetic storms over a span of 20 years, the composite model achieves an root mean square errors (RMSE) of 7.2 nT at 1 hr and 9.5 nT at 2 hr for predictions, which is comparable to recent models based solely on neural networks. Furthermore, the composite model can provide detailed information on the coefficients throughout the entire magnetic storm, which helps to elucidate the energy processes of the ring current during such events.

$$
\begin{aligned}
SYMH^*(t) &= SYMH(t) - b(t)P_S(t)^{(1/2)} \\
SYMH^*(t+\Delta t) &= \left(SYMH^*(t) - \frac{SYMH^*(t)}{2\tau_{loss}/\Delta t} - E_{in}\right)\left(1 + \frac{1}{2\tau_{loss}/\Delta t}\right) \\
SYMH(t+\Delta t) &= SYMH^*(t) + b(t+\Delta t)P_S(t+\Delta t)^{(1/2)}
\end{aligned} \tag{1}
$$

In this study, we will further optimize the composite model to enhance the accuracy of SYM-H predictions and explore the specific formula for the coupling function. Equation 1 presents the basic framework of the composite model for predicting the SYM-H index, where t represents the current time, Δt represents the prediction time interval (1 or 2 hr in this study), b is a dimensionless parameter, P_S denotes the solar wind dynamic pressure, and SYM-H* = SYM-H$-bP_S^{(1/2)}$ represents the magnetic field disturbance attributed to the ring current. τ_{loss} is the lifetime of ring current energetic particles due to charge exchange processes (with semi-implicit discretization used for the loss term). E_{in} represents the ring current energy injection during the time interval from t to $t + \Delta t$, which is directly related to the coupling function and results in a decrease in SYM-H during magnetic storms. Equation 1 is derived from the energy balance constraint of the ring current, where the temporal variation of SYM-H or the total energy of the ring current equals the energy injection minus the losses. The challenge lies in determining the parameters b, τ_{loss}, and E_{in}. Some empirical models use simple values or linear functions based on solar wind parameters and IMF to estimate these parameters, but this approach fails to capture the complex interactions between the solar wind and the magnetosphere. In this study, we employ neural networks to model these parameters, aiming to capture the complexity of the ring current evolution process and provide more accurate SYM-H predictions. Additionally, Equation 1 shows that the correlation between the SYM-H index and E_{in} is at least partially influenced by the loss process. Therefore, evaluating the coupling function solely based on this correlation cannot accurately assess the quality of different functional forms. The appropriate formula for the coupling function should be evaluated based on the model itself.

The parameters b and τ_{loss} in Equation 1 are determined by the neural network defined in the composite model. For the energy injection term, $E_{in} = c\int_t^{t+\Delta t} C_f dt$, where C_f represents the energy coupling function and c is an adjustment coefficient. In this study, we construct E_{in} based on the energy coupling function proposed by Wang et al., which was derived from their extensive simulation data using a PPMLR-MHD solar wind-magnetosphere coupling numerical model (Wang et al., 2014). Through dimensional analysis, they proposed the following expression for solar wind–magnetosphere energy injection:

$$C_f \sim n^{0.24} V^{1.47} B_T^{0.86} \left[\sin^{2.7}\left(\frac{\theta}{2}\right) + 0.25 \right] \tag{2}$$

where n is the solar wind particle number density, V denotes the solar wind velocity, $B_T = \sqrt{(B_Y^2 + B_Z^2)}$, and θ is the clock angle of the IMF. Based on Equation 2, we propose the following expression for the energy injection into the ring current:

$$E_{in} = cA \int_t^{t+\Delta t} n^{\gamma_1} V^{\gamma_2} B_T^{\gamma_3} \left[\sin^{\gamma_4}\left(\frac{\theta}{2}\right) + \beta \right] dt \tag{3}$$

where the scale parameters $\gamma_{1\sim4}$ and β are no longer predetermined constants but are variable and adjusted based on the model's performance in predicting SYM-H. The coefficient c is determined by the neural network because C_f represents the total energy injected into the magnetosphere, of which the ring current is only a part. Therefore, the energy that is ultimately injected into the ring current is not fixed and is characterized by c.

The machine learning library PyTorch is used to program the SYM-H prediction algorithm. As illustrated in Figure 1, we use fully connected neural networks to determine the parameters b and τ_{loss}. Please refer to Ji et al. (2023) for the specific network settings. The innovation in this study is that we use the solar wind–magnetosphere coupling function proposed by Wang et al. as a reference to construct the ring current energy input function. The scale factors $\gamma_{1\sim4}$ and β are set as trainable parameters with gradient information in PyTorch and embedded in the prediction program, allowing these scale factors to be determined during training with data. Additionally, the parameter c is obtained through the neural network, with the solar wind electric field and pressure as inputs.

The data set used in this study includes SYM-H and solar wind plasma parameters, such as the particle number density, solar wind velocity, and IMF, all with a time resolution of 1 minute. The data were obtained from the Space Physics Data Facility (SPDF) at NASA/GSFC. It is important to note that the model requires solar wind data from observations at the subsolar point of the magnetopause. However, continuous solar wind observations can only be achieved near the L1 point between the Earth and the Sun by spacecraft. The data from the SPDF were processed using a time-shifting algorithm, which estimates solar wind conditions at the subsolar point using observations at the L1 point. Additionally, during intense magnetic storms, solar wind plasma data are often missing for certain periods. To address this, linear interpolation is used to fill in the missing data. These storm data set were carefully selected, and according to our statistics, the proportion of bad data is very low. For the magnetic field data, the proportion of repaired bad data does not exceed 8%, and for plasma data, the proportion of repaired data is also less than 18%. Therefore, the impact of bad data repairs on the training of the model is limited. The training data set (Table 1) spans a complete 12-year period from 2000 to 2012 and includes 20 storms. The validation data set contains five storms, and the test data set comprises 13 storms. Each storm has a duration of approximately 10 days. For consistency with previous studies, the data set selected in this study aligns with those used in earlier research (Collado-Villaverde et al., 2021; Ji et al., 2023; Siciliano et al., 2021).

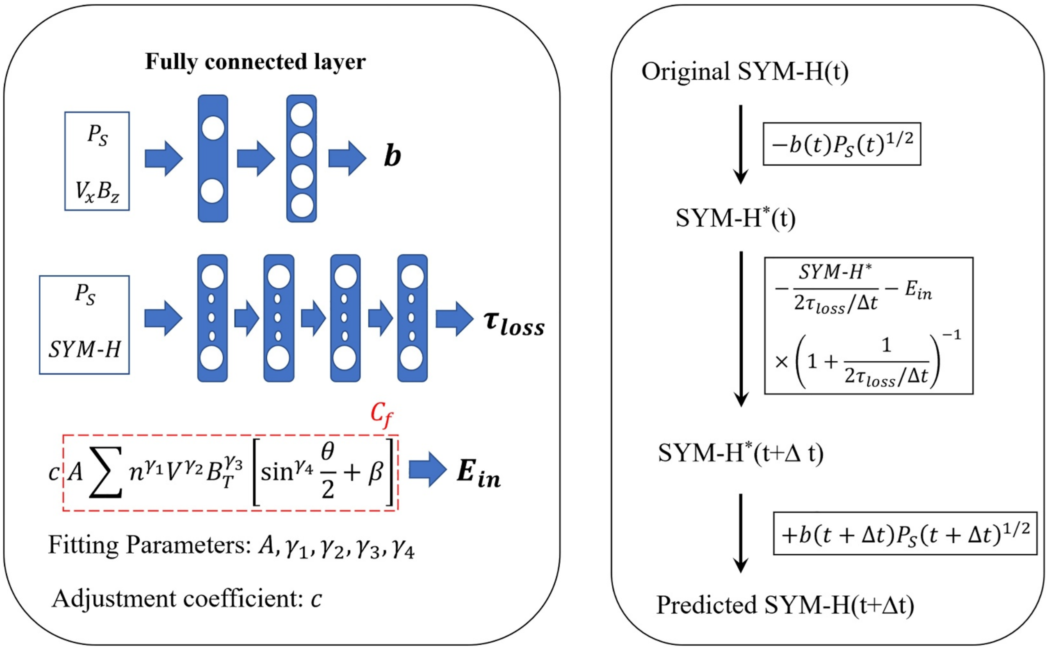

Figure 1. The SYM-H prediction algorithm.

The SYM-H prediction algorithm described in the above section is implemented using PyTorch. The training data set is used to optimize the neural network and the coefficients in the program. RMSE and the coefficient of determination R^2 are employed to evaluate the modle's performance. During training, we define the loss function as the RMSE between the SYM-H output (y) and its corresponding observation $(\hat{y})$.

$$RMSE(y, \hat{y}) = \sqrt{\frac{1}{n}\sum_{j=1}^{n}\left(y_j - \hat{y}_j\right)^2} \tag{4}$$

R^2 is a dimensionless metric defined as follows:

$$R^2(y, \hat{y}) = 1 - \frac{\sum_{j=1}^{n}\left(y_j - \hat{y}_j\right)^2}{\sum_{j=1}^{n}\left(y_j - \bar{y}_j\right)^2} \tag{5}$$

The Adam optimizer, a stochastic gradient descent algorithm, is used for continuous and iterative parameter optimization to minimize the RMSE. Training stops when the RMSE of the validation data set exceeds that of the training data set, serving as a precaution against overfitting. The learning rate is set to 0.01. Due to the relative simplicity of the networks in this study, each training session is completed in just a few tens of minutes, which is advantageous for experimenting with different network designs.

3. Results

Table 2 shows the RMSE and R^2 of the 1-hr model for predicting SYM-H from magnetic storms in the test data set. Results from Ji et al. (2023) are also included in Table 2 for comparison purposes. It is evident that for most magnetic storms with SYM-H values ranging from −100 nT to −300 nT, the composite model achieves an RMSE of approximately 3–8 nT. However, for two strong magnetic storms with minimum SYM-H values approaching −437 nT and −394 nT, the predicted RMSEs are much higher, about 11.7 and 11.4 nT, respectively. This discrepancy arises from a lack of training data for large magnetic storms, leading to insufficient accuracy in the determined parameters. The average RMSE and R^2 values for all tested magnetic storms are 6.7 nT and 0.954, respectively. Compared to Ji et al. (2023), this model reduces the RMSE by about 0.5 nT and increases R^2 by about 0.003. Notably, for the large magnetic storm 33, there is a significant improvement as its RMSE decreases

Table 1
Training Data Sets and Validating Data Sets Used in This Study

No.	Start date	End date	SYM-H_{min}(nT)
Train subset			
1	06/08/2000	16/08/2000	−235
2	15/09/2000	25/09/2000	−203
3	01/11/2000	15/11/2000	−176
4	14/03/2001	24/03/2001	−165
5	06/04/2001	16/04/2001	−280
6	17/10/2001	22/10/2001	−219
7	17/05/2002	27/05/2002	−116
8	15/11/2003	25/11/2003	−490
9	20/07/2004	30/07/2004	−208
10	02/01/2005	12/01/2005	−112
11	13/02/2005	23/02/2005	−95
12	03/03/2005	13/03/2005	−66
13	19/08/2005	29/08/2005	−179
14	01/04/2006	11/04/2006	−107
15	14/08/2006	24/08/2006	−95
16	20/09/2006	30/09/2006	−58
17	07/12/2006	17/12/2006	−211
18	05/03/2008	15/03/2008	−100
19	05/10/2008	15/10/2008	−65
20	01/03/2012	11/03/2012	−150
Validation subset			
21	01/04/2010	15/04/2010	−90
22	05/11/2010	15/11/2010	−55
23	18/06/2015	28/06/2015	−208
24	01/09/2017	11/09/2017	−146
25	05/05/2019	15/05/2019	−80
Test subset			
26	16/01/2000	26/01/2000	−101
27	02/04/2000	12/04/2000	−320
28	19/05/2000	28/05/2000	−173
29	26/03/2001	04/04/2001	−437
30	26/05/2003	06/06/2003	−137
31	08/07/2003	18/07/2003	−77
32	18/01/2004	27/01/2004	−137
33	04/11/2004	14/11/2004	−394
34	10/09/2012	05/10/2012	−138
35	28/05/2013	04/06/2013	−137
36	26/06/2013	04/07/2013	−111
37	11/03/2015	21/03/2015	−234
38	22/08/2018	03/09/2018	−206

from 13.9 to 11.4 nT after adopting the new energy coupling function, resulting in an approximate relative accuracy improvement of around 20%. The performance of this new model is better than that of previous neural network models developed by Siciliano and Collado-Villaverde but falls slightly short compared to SymHnet developed by Abduallah et al., which represents the latest advancement in this field. The advantage of this new model is that it allows for the analysis of the physical processes behind solar wind–magnetosphere interactions, which is beneficial for further improving the prediction accuracy of the model. Table 3 presents the RMSE and R^2 values obtained for the 2-hr model using the test data set and also includes the results from Ji et al. (2023) for comparison. Overall, the prediction accuracy of the 2-hr model is slightly lower than that of the 1-hr model, with an increase of about 2 nT in the RMSE and a decrease of 0.05 in R^2. This is reasonable because extending the prediction time introduces more random factors affecting the ring current energy process, which the new model cannot adequately capture. For storms with SYM-H values greater than −300 nT, the new model predicts SYM-H with an RMSE of less than 10 nT. However, for two extremely large storms (29 and 33), the errors are larger, with RMSE values of 14.7 and 14.8 nT, respectively. The average RMSE and R^2 for the test storms are approximately 8.9 nT and 0.949, respectively. Comparing these results with those obtained by Ji et al. (2023), our new composite model demonstrates improved performance, with an RMSE reduction of approximately 0.6 nT and an R^2 improvement of around 0.008. Similarly, the 2-hr model predictions outperform those of the neural network model developed by Siciliano and Collado-Villaverde, though they fall short compared to the results from Abduallah et al. To further investigate the performance of the new model, we analyzed four representative magnetic storms. Figure 2 illustrates the forecast results for magnetic storms 27, 29, 33, and 38. The red line represents the forecasted SYM-H index, the black line represents the observed values, and the blue line shows the difference between the predicted and observed values. The corresponding minimum SYM-H index values are −320 nT, −437 nT, −394 nT, and −206 nT, respectively. Generally, there is good agreement between the predictions and observations, particularly during quiet periods and the latter half of the recovery phase (slow recovery phase), with deviations of less than 10 nT. However, significant discrepancies occur during the sudden storm commencement (SSC), main, and early recovery phases. For storms 27 and 38, the maximum deviations reach about 50 nT, while for storms 29 and 33, which have larger magnitudes of around −400 nT, the maximum deviations are about 100 nT. These large errors occur within short time intervals and are characterized by pulsating positive or negative deviations. These errors are primarily caused by rapid variations in the solar wind impacting the magnetosphere during SSC. It is important to note that the initial solar wind data is obtained by translating observations from the L1 point to the magnetopause, which introduces potential errors not accounted for in this model, significantly affecting prediction performance.

Figure 3 shows details of the predicted SYM-H for typical magnetic storms using the 2-hr model. The selected magnetic storms are the same as those in Figure 2. In the figure, the black line represents the observed SYM-H, the red line represents the predictions, and the blue line represents the deviation between observations and predictions. The 2-hr model still provides better forecast results during quiet times, but significant deviations occur during the SSC and main phases. These deviations are notably larger than those observed with the 1-hr model, suggesting that discrepancies in the 2-hr model primarily

Table 2
Root Mean Square Errors and R^2 of the 1-hr Prediction Results Obtained by the Composite Model on the Test Data Set

	Ji et al. (2023)		This work	
No.	RMSE (nT)	R^2	RMSE (nT)	R^2
26	4.0	0.969	3.6	0.974
27	8.4	0.967	6.8	0.980
28	6.1	0.964	5.6	0.970
29	12.5	0.972	11.7	0.975
30	8.1	0.867	8.4	0.869
31	6.6	0.933	6.6	0.931
32	7.4	0.920	7.7	0.912
33	13.9	0.971	11.4	0.981
34	3.9	0.939	3.7	0.946
35	5.3	0.953	5.5	0.948
36	4.3	0.971	4.4	0.972
37	8.1	0.965	7.1	0.974
38	5.0	0.972	4.8	0.976
Mean	7.2	0.951	6.7	0.954

Note. The left column takes the interplanetary electric field E_y as the energy coupling function, and the right column takes the result of Equation 3 as the energy coupling function.

Table 3
Root Mean Square Errors and R^2 of the 2-hr Prediction Results Obtained by the Composite Model on the Test Data Set

	Ji et al. (2023)		This work	
No.	RMSE (nT)	R^2	RMSE (nT)	R^2
26	5.3	0.946	4.9	0.952
27	12.0	0.923	9.8	0.956
28	8.3	0.931	7.4	0.943
29	14.4	0.961	14.7	0.961
30	10.1	0.788	10.4	0.801
31	8.5	0.895	8.2	0.893
32	9.7	0.864	10.6	0.838
33	18.1	0.951	14.8	0.968
34	5.4	0.879	4.8	0.905
35	9.2	0.911	7.3	0.905
36	5.4	0.955	5.7	0.952
37	11.7	0.929	9.3	0.952
38	7.4	0.936	7.1	0.949
Mean	9.5	0.913	8.9	0.921

Note. The left column takes the interplanetary electric field E_y as the energy coupling function, and the right column takes the result of Equation 3 as the energy coupling function.

arise from the SSC and main phases. Therefore, future models should focus on a detailed analysis of the SSC and main phases to identify the causes of these deviations and optimize the model accordingly.

Figures 4a and 4b shows scatter plots of the predicted SYM-H (vertical axis) versus the observed SYM-H (horizontal axis) for (a) the 1-hr model and (b) the 2-hr model. The plots include data from four magnetic storms: 27 (magenta squares), 29 (green diamonds), 33 (black circles), and 38 (blue triangles), consistent with the data shown in Figures 2 and 3. The red line represents the line of equality (x = y), which is used to evaluate the prediction accuracy. The forecast results for the 2-hr model are more dispersed than those of the 1-hr model, indicating that the 2-hr predictions are of lower accuracy. For sample points where SYM-H >0 nT, most fall below the red line with relatively large dispersion, suggesting poor prediction accuracy during the SSC of magnetic storms. This indicates that the contribution of SYM-H from the magnetopause current, which is influenced by the dynamic pressure balance, is not quantified well and requires further improvement.

In contrast, for sample points within the −200 to 0 nT range, the data are closely clustered around the red line, indicating good agreement between predictions and observations in this range. However, for sample points below −200 nT (mostly corresponding to storms 29 and 33), the distribution starts to deviate from the red line, suggesting a deterioration in model performance and decreased prediction accuracy. Comparing our results with those of Ji et al., who used the interplanetary electric field as an energy injection function, shows that our approach improves performance by addressing a common insufficient injection in previous models (Cai et al., 2010; Siciliano et al., 2021) — the prediction of larger SYM-H values than those observed during severe magnetic storms. This indicates that the new energy injection term using the coupling function expression effectively captures the influence of solar wind parameters on ring current energy injection.

To evaluate the performance of the new model, the solar wind conditions of magnetic storm 29, along with the corresponding terms in Equation 1 and the predicted SYM-H, are displayed in Figures 5 and 6. Figure 5a shows the temporal variation of the solar wind dynamic pressure (calculated by $P_S^{1/2} = \left(2\mu_0 P_{SW}\right)^{1/2}$) throughout the magnetic storm. Here, solar wind dynamic pressure is expressed in units of nT for ease of comparison. Figure 5b provides a detailed depiction of the observed SYM-H index. The solar wind dynamic pressure fluctuates significantly during the storm, ranging from 50 to 300 nT, with sudden increases and decreases corresponding to shock wave structures in the solar wind. Similarly, the SYM-H index increases and decreases in sync with these variations in dynamic pressure, as the magnetopause current, determined by the solar wind dynamic pressure, also affects the observed SYM-H. Notably, around the fifth day, the dynamic pressure surged to 300 nT, causing a sudden commencement in SYM-H; subsequently, the dynamic pressure stabilized at approximately 200 nT while SYM-H entered the main phase and rapidly dropped to −400 nT. Figure 5c shows the changes in the parameter b during the magnetic storm, where the red line represents the 1-hr model result and the blue line represents the 2-hr model result. Both are around 0.25, slightly higher than the 0.2 value in the BMR model. The parameter b is the scaling factor that represents the contribution of the magnetopause current to the SYM-H index. During quiet periods, the magnetopause current is relatively distant from the Earth's surface and remains stable, resulting in a small and nearly constant value of b, with only

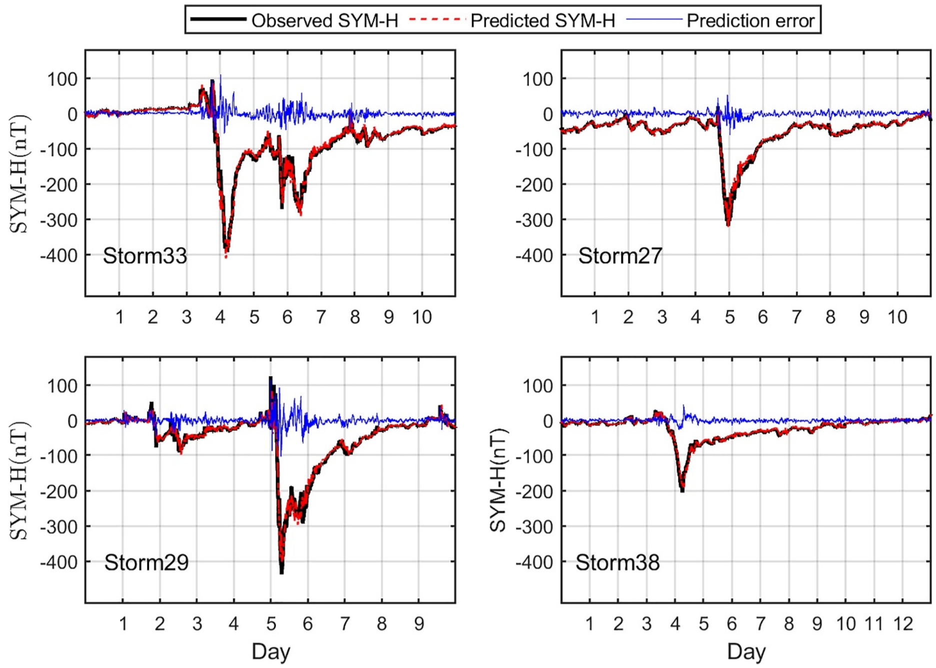

Figure 2. A comparison of the predicted (red line) and observed (black line) SYM-H of the composite model over 1 hr for different individual storms. The blue line represents the predicted SYM-H minus the observed value.

slight variations occurring during geomagnetic storms. Figure 5d shows the time variation of SYM-H*, where SYM-H* = SYM-H$-bP_S^{(1/2)}$ represents the disturbance with the contribution of the magnetopause current removed. SYM-H* exhibits a slight decrease compared to SYM-H while maintaining a similar trend. The discontinuity at SSC points is less pronounced. However, it is important to note that SYM-H* is not always less

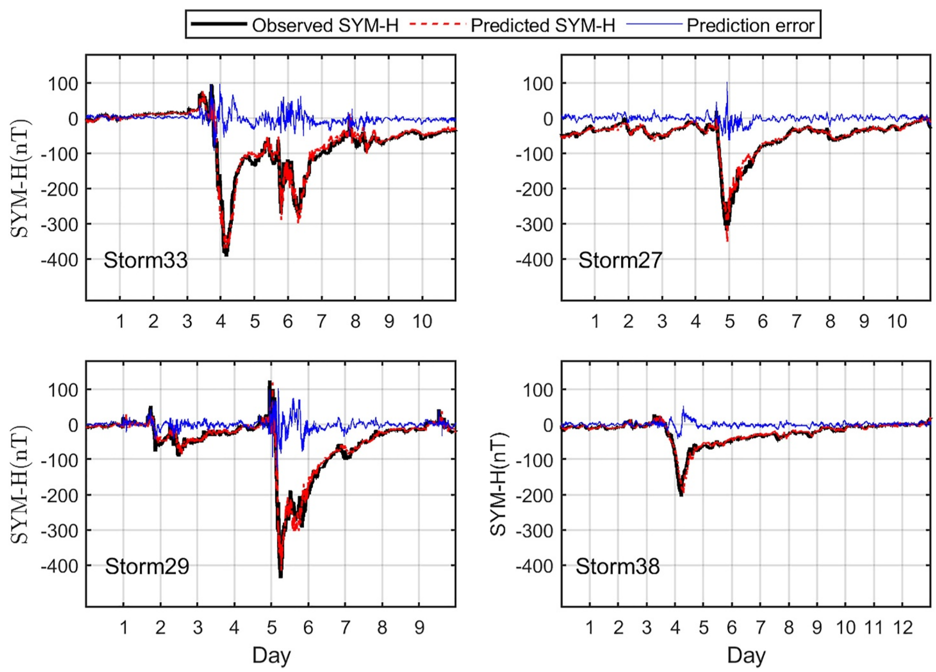

Figure 3. A comparison of the predicted (red line) and observed (black line) SYM-H from the composite model over 2 hr for different individual storms. The blue line represents the predicted SYM-H minus the observed value.

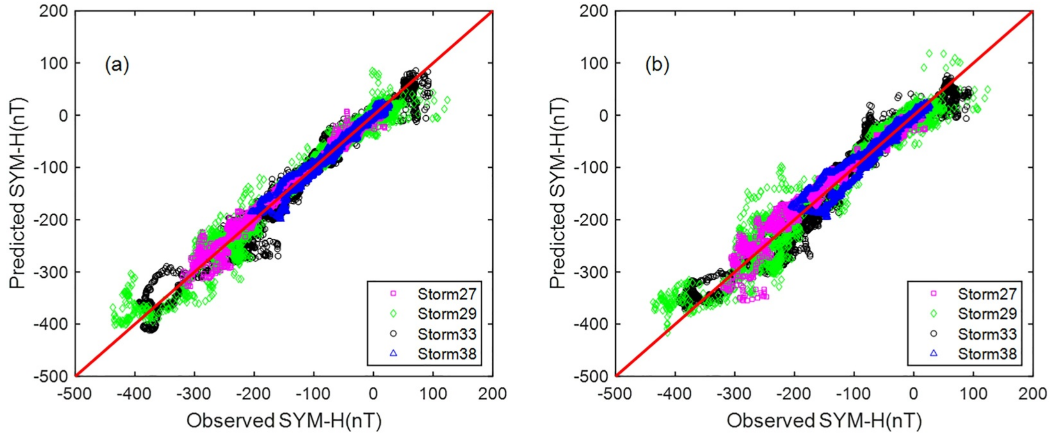

Figure 4. A scatter plot of the observed and predicted SYM-H indices from the composite model, (a) for the 1-hr prediction and (b) for the 2-hr prediction.

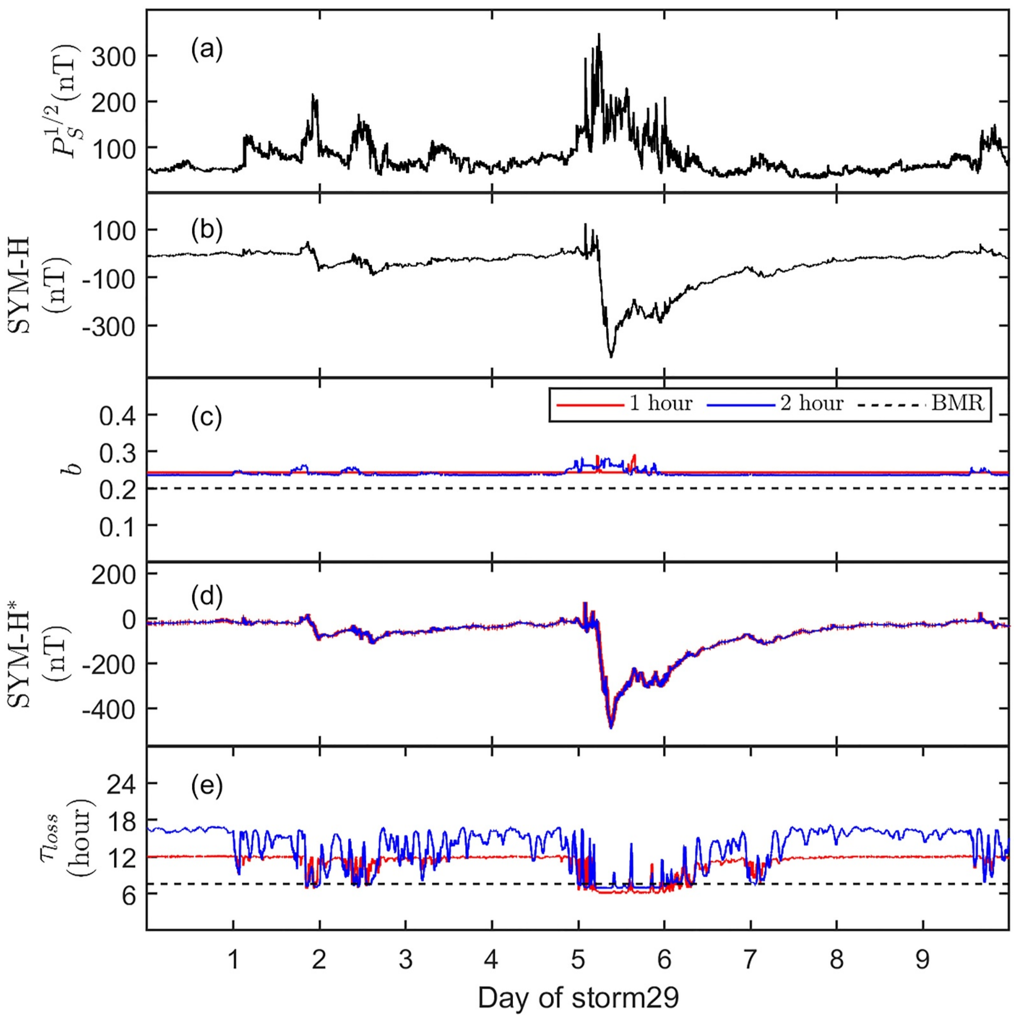

Figure 5. Inputs and outputs of the neural network on magnetopause current correction and τ_{loss} during storm 29. The (a) solar wind dynamic pressure in units of nT, (b) the SYM-H index, (c) parameter b from Equation 1, (d) SYMH* after deducting the contribution of the solar wind dynamic pressure, and (e) the lifetime of the ring current particles. The red line is the 1-hr model result, and the blue line is the 2-hr model result.

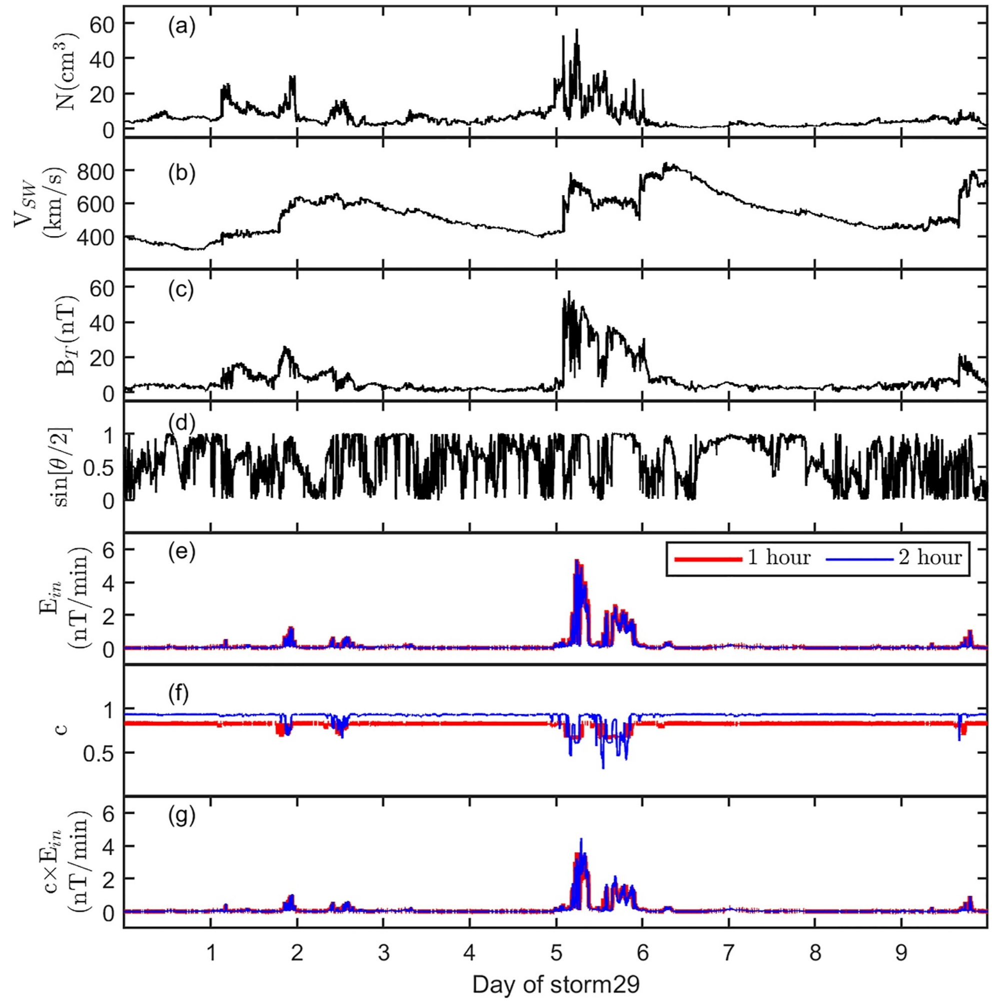

Figure 6. The solar wind parameters and ring current energy injection function. (a) The solar wind number density, (b) the solar wind velocity, (c) the magnetic field in the Y–Z plane, (d) the clock angle, (e) the energy coupling function corresponding to Equation 2, (f) the correction factor of the energy injection function, and (g) the energy injection rate of the ring current.

than zero. During the magnetic storm SSC, there are instances when SYM-H* is still greater than zero, indicating that the correction for removing the effect of the magnetopause current needs improvement, as ring currents should only yield negative SYM-H*. Figure 5e shows the lifetime of ring current particles, which is approximately 12 hr during quiet times for the 1-hr model and 17 hr for the 2-hr model. During magnetic storms, both models yield similar results of around 6–7 hr, consistent with the BMR model. During quiet periods, the particle composition and structure of the ring current are relatively stable, so the average lifetime of particle τ_{loss} also remains nearly constant, which is consistent with physical expectations.

Equation 3 is derived from the coupling function given by Wang et al. (2014), which is based on MHD numerical simulations. In this formula, the scale exponents from Wang et al.'s (2014) coupling function are set as adjustable parameters. The values of each parameter, after training on observations, are shown in Table 4.

The parameters in Equation 3 determined by the 1-hr and 2-hr models are similar, except for β, which characterizes the rate of solar wind energy injection into the magnetosphere during quiet times. Compared to the values provided by Wang et al. (2014), the scaling exponents for the particle number density n and $\sin\left(\frac{\theta}{2}\right)$ show significant variation. Specifically, one exponent increases from 0.24 to approximately 0.45, while the other rises from 2.7 to around 8.0.

Table 4
The Concrete Equations for the Energy Injection Functions of Different Models

Model	γ_1	γ_2	γ_3	γ_4	β	Equation
1-hr	0.43	1.74	0.92	7.8	0.09	$C_f \sim n^{0.43} V^{1.74} B_T^{0.92} \left[\sin^{7.8}\left(\frac{\theta}{2}\right) + 0.09\right]$
2-hr	0.46	1.73	0.91	8.3	0.06	$C_f \sim n^{0.46} V^{1.73} B_T^{0.91} \left[\sin^{8.3}\left(\frac{\theta}{2}\right) + 0.06\right]$

Figure 6 shows the solar wind parameters and the corresponding ring current energy injection function in Equation 3 during storm 29. Figure 6a shows the variation in the solar wind number density. Most of the time, the value remains below 10 cm^{-3}. During a minor magnetic storm (on the 2nd day), N increases to approximately 20 cm^{-3}. During the major magnetic storms (between the 5th and 6th days), N rises significantly to nearly 60 cm^{-3} and remains elevated for an extended period. Figure 6b shows the solar wind velocity, which ranges from 300 km/s to 800 km/s. At the start of the large storm, the solar wind velocity suddenly increases to more than 600 km/s. Compared to N, the variation in the solar wind velocity is less pronounced, with the maximum value being about twice the minimum value. Figure 6c shows the magnetic intensity in the Y–Z plane. During quiet periods, B_T remains below or equal to 10 nT. At the start of the magnetic storm, B_T rapidly increases to beyond 40 nT, peaks close to 60 nT, and remains elevated throughout the main phase. Figure 6d shows the variation in $\sin\left(\frac{\theta}{2}\right)$, which oscillates between zero and one. During the main phase, $\sin\left(\frac{\theta}{2}\right) = 1$, indicating that the southern component of the solar wind magnetic field B_Z is dominant and the injection of ring current energy effective. Figure 6e shows the energy injection function calculated using the parameters and formula given in Table 3. The unit used here is nT/min, which indicates by how many nT per minute the injected energy can reduce the SYM-H index. Most of the time, the energy injection function is less than 1 nT/min. It increases significantly at the onset of the magnetic storm, reaching about 6 nT/min during the main phase. After entering the recovery phase, it remains at around 4 nT/min for a period of time. Meanwhile, SYM-H remains unchanged at −200 nT, as shown in Figure 5b. Figure 6f shows the corrected coefficient of energy injection of the ring current, denoted as c in Equation 3, and indicates that the energy injection also depends on the state of the magnetosphere. Other than during the recovery phase and quiet times, the scaling coefficient remains close to unity for both the 1-hr and 2-hr models. During magnetic storms, c decreases slightly to around 0.7 for both models. During quiet periods, the injection of ring current energy is quite stable, so the parameter c remains unchanged. Figure 6g shows the net energy injection given by Equation 3. The energy injection is usually less than 1 nT/min, but during the magnetic storm, it reaches about 4 nT/min.

4. Discussion

The ring current plays an important role in the magnetospheric current system, with its intensity modulated by the solar wind. Plasma and energy from the solar wind can be injected into the inner magnetosphere, leading to an increase in the total energy and intensity of the ring current and a rapid decline in the SYM-H index. This study presents a model for predicting SYM-H based on the total energy balance of the ring current (Burton et al., 1975; Ji et al., 2023). Specifically, the solar wind–magnetosphere energy coupling function proposed by Wang et al. (2014) is used as the energy injection function in the model, with the scaling exponents optimized. The forecast accuracy of the new model is improved by about 7%(1-hr) and 6% (2-hr) over that of Ji et al. (2023). The predicted RMSE decreases significantly for severe magnetic storms, and the tendency for the predicted SYM-H to be larger than the observed SYM-H during the main phase of large storms is eliminated. The improved prediction results indicate that the new energy injection function can more accurately describe the plasma and energy transport process from the magnetotail to the ring current during a magnetic storm. We will discuss the physical significance of the model parameters and analyze the sources of prediction errors in this section.

4.1. Energy Injection Function

During a magnetic storm, the energetic particles in the ring current are primarily injected from the magnetotail current sheet. Therefore, the energy injection function is closely related to both the plasma state of the current sheet and the intensity of the driving electric field. Moreover, the solar wind conditions directly influence the plasma state within the current sheet. Consequently, this model facilitates the identification of a quantitative relationship between the ring current energy injection function and the solar wind parameters. Borovsky et al. (1998) used observations of many years from various satellite pairs find statistical relations between the solar wind and current sheet as follow: $n_{CS} = 0.292 n_{SW}^{0.49}, T_{CS} = 2.17 + 0.0223 V_{SW}$ which are also widely used as boundary conditions in ring current numerical mode (Y. Yu et al., 2024) Therefore, the scaling exponent of C_{in} with respect to n should be 0.5 0.49, which is very close to the 0.43 and 0.46 found for the model. Furthermore, C_{in} shows a linear correlation with the kinetic energy or temperature associated with the thermal motion of particles within the current sheet, while the temperature in this region shows a linear dependency on v_{SW} (solar wind velocity). Thus, C_{in} depends linearly on v_{SW} according to the relationship between the temperature and solar wind velocity. When the B_Z component of the IMF is pointing southward, magnetopause reconnection occurs. To ensure the conservation of magnetic flux during reconnection, the driving electric field must satisfy $E_y = v_{SW} B_z$. Consequently, the energy injection also depends linearly on E_y, so $C_{in} \sim v_{SW} B_z$. The contributions of the current sheet temperature and the driving electric field to the energy injection of the ring current are essentially independent. When considered together, their combined effect is approximately multiplicative, meaning $C_{in} \sim n^{0.49} v_{SW}^2 B_Z$. If the southward IMF is dominant, then $C_{in} \sim n^{0.49} v_{SW}^2 B_Z$ also holds true. This expression closely aligns with the values presented in Table 3, which were derived from data after training, demonstrating that the new model accurately captures the underlying physical laws.

Note that the scaling factors for $\sin\left(\frac{\theta}{2}\right)$ in the 1-hr and 2-hr model formulas in Table 3 are 7.8 and 8.3, respectively. These values are significantly higher than the 2.7 reported by Wang et al. (2014) and other researchers. A larger scaling factor indicates that substantial energy injection occurs only when the B_Z component is strongly dominant in the IMF (i.e., $\sin\left(\frac{\theta}{2}\right) \approx 1$). Conversely, when $\sin\left(\frac{\theta}{2}\right) < 1$, the final value approaches zero due to multiple exponentiation, implying that energy entering the magnetosphere is less likely to be injected into the ring current region. This also suggests that the energy coupling functions vary for different magnetospheric energy processes. During substorms, energy dissipation primarily occurs in the cusp region with minimal energy injection (Akasofu, 1981). In contrast, during magnetic storms, energy is dissipated in the deeper ring current region with substantial energy injection, requiring more stringent solar wind conditions (a high IMF dynamic pressure and dominant B_Z) to achieve effective energy injection.

In addition, the β values for the 1-hr and 2-hr models are significantly lower than the 0.25 reported by Wang et al. (2014), with respective values of 0.09 and 0.06. The parameter β characterizes the energy injected into the inner magnetosphere via the diffusion process, which accounts for about 10% of the convective energy injection ($\sim$1). Furthermore, Wang et al.'s (2014) coupling function represents energy penetration at the magnetopause, while this study focuses on energy injection into the ring current within the inner magnetosphere. Consequently, the energy transport due to the diffusion process is less significant than that due to the convective process, resulting in a smaller β than that reported by Wang et al. (2014). The discrepancy between the 1-hr model (0.09) and the 2-hr model (0.06) may be attributed to truncation errors associated with the discrete format.

In the composite model, the energy injection described by the formula in Table 4 is not entirely directed into the ring current. The expression for E_{in} includes a regulatory factor c, which controls the final proportion of energy injected into the ring current. Figure 6f shows that during the main phase, the coefficient c is smaller than during quiet times, indicating that some of the injected energy is lost during the magnetic storm. This is because an enhanced convection electric field and the compression of the magnetopause during a magnetic storm can cause a portion of the ring current energetic particles to drift directly out of the magnetopause after being injected from the magnetotail. Therefore, not all of the injected energy contributes to forming a symmetric ring current. The time scale of this loss is roughly equivalent to the time it takes for the energetic ring current particles to drift from the magnetotail to the sunward magnetopause, as also discussed by Ji et al. (2023). In addition, if substorms occur concurrently with magnetic storms, they will contribute to the energy budget associated with substorms, which is not accounted for in the current model. A comprehensive model should fully consider all energy inputs and losses and be capable of simultaneously predicting both the SYM-H index and the AL index. However, the relationship between magnetic storms and substorms remains inconclusive. To develop a more advanced model, it is necessary to incorporate neural networks to capture the nonlinear interactions between them.

Another advantage of the composite model is its use of the energy coupling function to construct a quantitative model, thereby providing an effective method to identify an accurate formula for the coupling function. Moreover, while the general form of the coupling function is similar for different geomagnetic disturbance parameters, the scale exponents should vary. A practical energy coupling function should be tested within the model. Regarding ring current dynamics, since the composite model specifies the exact form of the energy injection function based solely on solar wind parameters, we can calculate potential changes in the SYM-H index at any position along the Sun–Earth line (as depicted in Figure 6e) and estimate arrival times at Earth based on the solar wind speed. This capability allows researchers to predict future magnetic storm intensities, which is of great significance for space weather forecasting. The composite model not only provides precise SYM-H predictions within 1–2 hr but also establishes an accurate relationship between solar wind parameters at any location and their corresponding influence on energy injection into Earth's magnetospheric ring current.

4.2. The Lifetime of Ring Current Particles

The recovery phase is primarily characterized by the decay of the ring current's total energy. During this phase, the SYM-H index gradually returns from the minimum to its normal value. Understanding the dynamics of the recovery phase is crucial for space weather prediction. SYM-H observations reveal that the recovery phase can be divided into two parts: a fast recovery phase and a slow recovery phase. The total energy loss time, τ_{loss}, obtained from the composite model also reflects the fast and slow recovery phases. In Figure 5e, the blue and red lines represent τ_{loss} as measured by the 1-hr and 2-hr models, respectively. During quiet times and the slow recovery phase, both models estimate τ_{loss} to be greater than 10 hr — specifically, τ_{loss} is 12 hr for the 1-hr model and 17 hr for the 2-hr model. However, both models yield similar results during the main phase of magnetic storms with a τ_{loss} value of approximately 7 hr, which is consistent with the BMR model (dashed line).

The formation of fast and slow recovery phases can be explained as follows: during a large magnetic storm, the increased influx of oxygen ions from the ionosphere energizes them and injects them into the ring current. As a result, the main component of the ring current energy gradually shifts from hydrogen ions to oxygen ions. The cross-sectional area for charge exchange between oxygen ions and neutral atoms is larger than that for hydrogen ions, meaning that oxygen ions experience less lifetime through charge exchange than hydrogen ions. After the main phase, oxygen ions rapidly lose energy, followed by a slower loss of hydrogen ions, leading to a fast recovery and a slow recovery of the SYM-H index. Observations and numerical simulations support this interpretation (Daglis et al., 1999; Fok et al., 1991; Yue et al., 2019). However, the loss of energetic particles in the ring current involves complex processes, including ionospheric particle precipitation, plasma Coulomb collisions, and magnetopause drift loss, all of which also influence the formation of the fast or slow recovery phase.

In addition, the τ_{loss} provided by the 1-hr composite model is 12 hr, which is significantly lower than the 17 hr reported for the 2-hr model. This discrepancy arises from differences in the time advancement steps, which correspond to variations in β within the ring current energy injection function (as specified in Table 4). Assuming that the IMF has no southward component during quiet times, the energy balance of the ring current primarily depends on the diffusion-induced energy input (represented by the parameter β) and loss equilibrium. We can then define

$$SYMH_{eq} = -E_{in} \times \tau_{loss} \tag{6}$$

where SYM-H_{eq} is the equilibrium value given by the quiet time observation data, so the 1-hr and 2-hr values should be the same. The difference in time step does not affect the validity of the above formula. At this time, the product of $E_{in} \times \tau_{loss}$ for the 1-hr model is equal to that of the 2-hr model, that is, $0.09 \times 12 \approx 0.06 \times 17$. This supports the conclusion that the difference in time step is the reason for the variation in β and E_{in}.

4.3. Errors

The composite model demonstrates a satisfactory level of prediction accuracy for SYM-H. However, it is important to discuss the underlying factors contributing to these discrepancies in order to enhance the model's accuracy.

4.3.1. Effects of Substorms

The substorm process releases large amounts of energy into the magnetospheric system including to the ring current (Jang et al., 2021; Sandhu et al., 2018). H. Fu et al. (2023) found that intense substorms can also cause a $\sim 3nT/Hr$ geomagnetic decrease. Figure 7 shows the variation curves of the SYM-H index and the AL index,

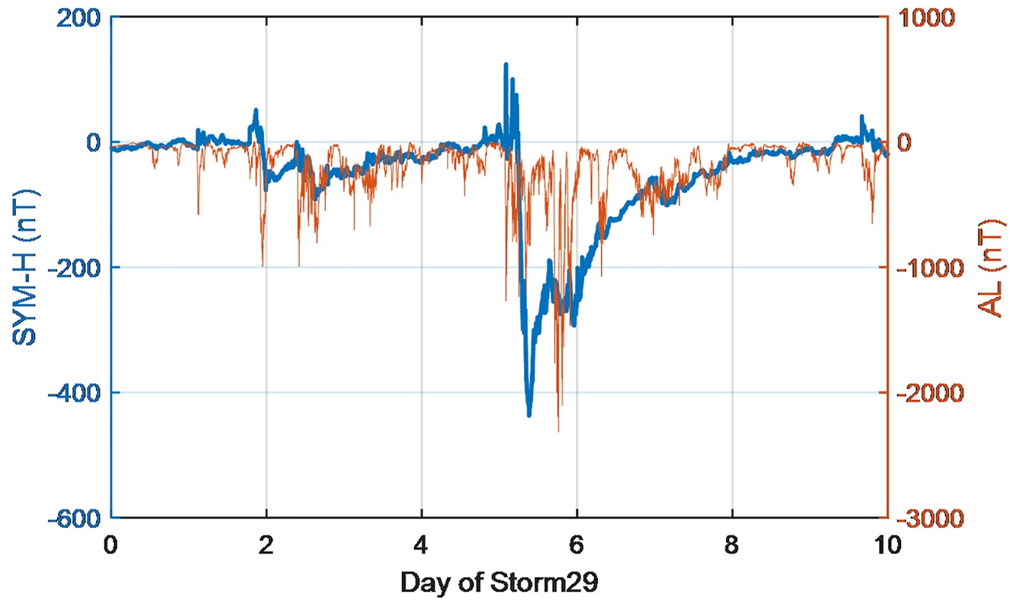

Figure 7. The SYM-H and AL index during Storm 29.

using magnetic storm 29 as an example. The AL index primarily indicates the intensity of nightside substorm activity. There is a strong correlation between changes in SYM-H and the AL index, with significant variations in SYM-H often accompanied by substantial changes in the AL index. Substorm activity exhibits some degree of randomness, which is not accounted for in the current model and may lead to errors. Shen et al. (2002) estimated the intensity of the driving electric field on the night side using the AL index and ionospheric parameters, calculated the ring current energy injection, and proposed a quantitative model relating the SYM-H and AL indices. These concepts could provide valuable avenues for enhancing our composite model.

To investigate the energy contribution of substorms to ring current, we attempted to use the AL and AU indices as inputs to the neural network to modulate the energy injection into the ring current in the model. However, we found that incorporating substorm indices did not improve the model's performance. We speculate that this is because substorms are relatively stochastic processes and do not necessarily lead to an increase in ring current energy. Therefore, a simple fully connected neural network is insufficient to represent the relationship between geomagnetic storms and substorms. To account for the influence of substorms, a more complex model structure is required, one that incorporates stochastic mechanisms. This exceeds the capability of the current model and will be the focus of our future work.

4.3.2. Response Time

The energy injection function of the composite model is calculated from the prevailing solar wind conditions at the magnetopause. However, the actual solar wind does not directly penetrate the sunward magnetopause to enter the ring current but first enters the magnetotail before being injected. This process introduces a time delay of 20~30 min (Beharrell & Honary, 2016; Maggiolo et al., 2017; Palmroth et al., 2006) that the current model does not account for, which can lead to certain errors.

Regarding the time delay of the SYM-H index relative to solar wind conditions, we adjusted the model's energy injection to Equation 7:

$$E_{in} = cA\int_{t-\tau}^{t+\Delta t-\tau} n^{\gamma_1} V^{\gamma_2} B_T^{\gamma_3}\left[\sin^{\gamma_4}\left(\frac{\theta}{2}\right)+\beta\right]dt \tag{7}$$

where τ is the delay time. For time delay equating 10 min, the RMSE of predictions show a little decrease, but for time delay 20 and 30 min, the RMSE of predictions become even more larger (Table 5), indicating that during

10.1029/2024SW004160

Table 5
The RMSE of 1-hr Model After Considering Time Delay of Solar Wind Into Ring Current

No.	10 min delay	20 min delay	30 min delay
26	3.6	3.9	3.9
27	7.0	7.4	7.3
28	5.2	5.6	5.6
29	11.5	13.7	14.0
30	8.6	8.4	8.3
31	6.4	6.4	6.4
32	7.6	7.8	7.8
33	11.1	11.8	12.7
34	3.7	3.6	3.6
35	5.3	5.1	5.4
36	4.3	4.5	4.4
37	7.0	6.9	7.1
38	4.8	4.7	4.6
Mean	6.6	6.9	7.0

Note. Delay time (\tau = 10, 20, 30) minutes.

magnetostorm, the time delay of solar wind from magnetopause to magnetail is about 10 min, no more than 20 min.

4.3.3. Errors in Solar Wind Observations

Solar wind observations are not completely accurate, which contributes to errors in the model. Observation satellites cannot be positioned at the subsolar point of the magnetopause, and solar wind data are derived from satellites located near the solar–Earth Lagrange point. This inevitably results in deviations, particularly in shock wave structures, where even minor discrepancies can lead to significant errors. Figure 8 shows the predicted SYM-H values, observed values, corresponding errors, and solar wind dynamic pressure. The position indicated by arrow A corresponds to the sudden commencement of the magnetic storm and also to a break in the solar wind dynamic pressure. There is a noticeable time difference between the green line (solar wind dynamic pressure) and the black line (SYM-H), which causes the model to struggle with the SSC position. This results in a significant forecast error after 1 hr, as indicated by arrow B in Figure 8. The frequent discontinuities in the solar wind dynamic pressure during magnetic storms contribute to large deviations in the forecast results.

In addition, some of the larger deviations are related to sudden changes in SYM-H on small time scales, while the corresponding solar wind dynamic pressure shows no significant variations. This indicates that such changes are not caused by solar wind dynamic pressure but rather by transient processes occurring within the magnetosphere. Possible processes include significant drift loss of ring current particles at the magnetopause, disruptions in the magnetotail current sheet, and field-aligned currents. The current model cannot accurately capture these physical processes. In the future, we will consider integrating these processes into our model. For now, we have made minor improvements to the model in an attempt to reduce these deviations. Specifically, we corrected the current SYM-H* by constructing a neural network that uses the solar wind parameters and SYM-H index from the preceding 20 min as inputs, with the output being the corrected $SYMH^{*}(t) = SYMH(t) - b(t)P_S(t)^{(1/2)} + f$, where f is the corrected term. The Table 6 shows the RMSE results of the neural network's predictions after the

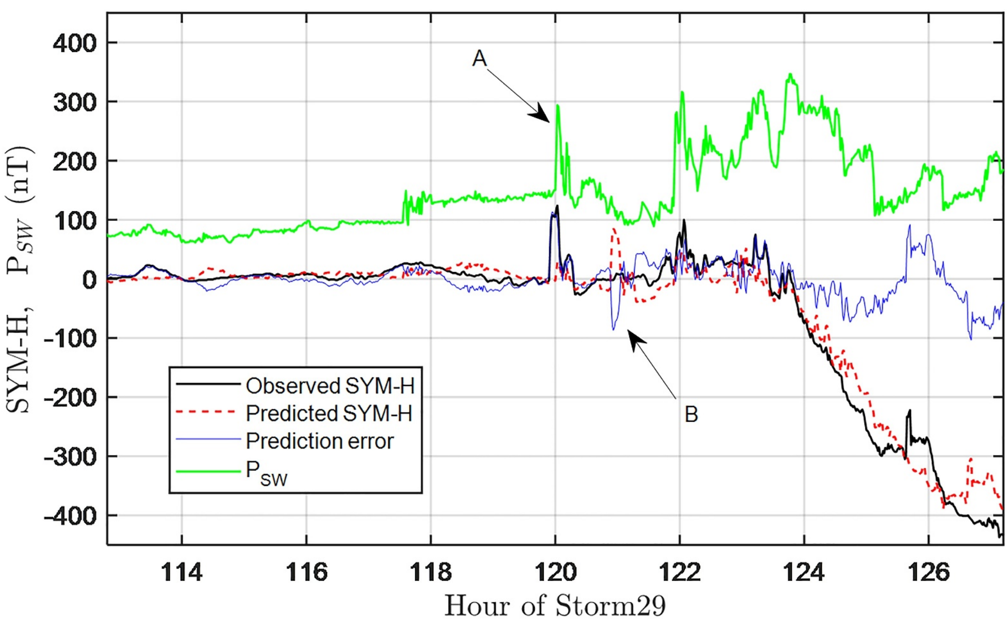

Figure 8. For Storm 29, the figure shows the predicted SYM-H values (red dashed line), observed SYM-H (black line), the errors between the predicted and observed values (blue line), and the solar wind dynamic pressure (green line).

Table 6
*The Root Mean Square Errors of 1-hr Model After Considering Correction of SYM-H**

No.	RMSE
26	3.6
27	6.6
28	5.2
29	11.5
30	7.9
31	6.2
32	7.6
33	11.2
34	3.6
35	5.3
36	4.1
37	6.9
38	4.7
Mean	6.5

correction. It can be seen that the results have indeed improved by approximately 3%. However, achieving further optimization will require more in-depth research.

5. Conclusion

In this study, we aim to further optimize the composite model for predicting the SYM-H index based on the energy balance approach proposed by Ji et al. (2023). Specifically, we have developed a novel ring current energy injection function based on the existing solar wind - magnetosphere energy coupling function, which follows a multi-parametric form derived from interplanetary solar wind plasma parameters. The parameters of the energy injection function and the ring current particle lifetime function were determined through training with 20 magnetic storm observations of solar wind and SYM-H data. Compared to the original composite model, the modified model demonstrates enhanced accuracy in both 1-hr and 2-hr SYM-H predictions, with the new RMSEs of 6.9 and 8.9 nT, respectively, representing an improvement of approximately 0.5 nT. Furthermore, in addition to providing improved prediction accuracy, the new model identifies the scale exponents in the ring current energy injection function. This enables direct calculation of the SYM-H decline rate for space weather predictions using solar wind parameters. Moreover, the determined exponents are consistent with the observation about dependence of plasma parameters in the magnetic tail current sheet on the solar wind conditions (Borovsky et al., 1998), demonstrating that the new physically-based model effectively captures the laws governing large-scale processes related to solar wind–magnetosphere interactions from a macroscopic perspective. The estimated lifetime of the fast recovery phase from the new model is approximately 6 hr, while the slow recovery phase takes more than 10 hr, consistent with previous analyses. It should be noted that the particle lifetime obtained here is a combined effect of all particles, and the current model does not distinguish the contributions of different types of ring current particles. Future research will focus on modeling the different components of ring current particles separately, aiming to uncover the true physical laws from historical observational data. This approach is expected to better capture the physical processes governing ring current evolution and provide improved forecasting results. Furthermore, the model's prediction accuracy remains insufficient when sudden changes in SYM-H occur due to certain shock structures in the solar wind, abrupt loss in magnetopause, or other transient large scale current structures in the magnetophere. This is a primary source of errors in the composite model which need further study.

Data Availability Statement

Data including IMF, particle number density, velocity fields in solar wind, and SYM-H index from 2000 to 2019 are downloaded from the NASA/GSFC' Space Physics Data Facility's OMNI Web service (https://cdaweb.gsfc.nasa.gov/pub/data/omni/). The description of high resolution OMNI data set can be found at (https://cdaweb.gsfc.nasa.gov/misc/NotesO.html#OMNI_HRO_1MIN) .

Acknowledgments
This work was supported by the National Key Research and Development Program of China (2022YFA1604600), the National Natural Science Foundation (NSFC) of China (Grants 42130202), Ningxia Natural Science Foundation (2024AAC03080). We are grateful to OMNI for providing us with data. The data and code files used in this paper can be found at https://doi.org/10.5061/dryad.1zcrjdfww.

References

Abduallah, Y., Alobaid, K. A., Wang, J. T. L., Wang, H. M., Jordanova, V. K., Yurchyshyn, V., et al. (2024). Prediction of the SYM-H index using a bayesian deep learning method with uncertainty quantification. *Space Weather-the International Journal of Research and Applications*, *22*(2). https://doi.org/10.1029/2023SW003824

Ahmad, N., Shen, C., Ji, Y., E, P., Rehman, U., Yao, G.-R., et al. (2025). The geometrical features of magnetic flux entanglement events observed by MMS. *Journal of Geophysical Research: Space Physics*, *130*(1), e2024JA033305. https://doi.org/10.1029/2024JA033305

Akasofu, S. I. (1981). Energy coupling between the solar wind and the magnetosphere. *Space Science Reviews*, *28*(2), 121–190. https://doi.org/10.1007/BF00218810

Axford, W. I. (1969). Magnetospheric convection. *Reviews of Geophysics*, *7*(1–2), 421–459. https://doi.org/10.1029/RG007i001p00421

Baker, D. N., Klimas, A. J., & Vassiliadis, D. (2007). Nonlinear dynamics in the Earth's magnetosphere. *Nonlinear Dynamics in Geosciences*, 53–67. https://doi.org/10.1007/978-0-387-34918-3_4

Barenblatt, G. I. (1996). *Scaling, self-similarity, and intermediate asymptotics: Dimensional analysis and intermediate asymptotics*. Cambridge University Press. https://doi.org/10.1017/CBO9781107050242

Bargatze, L., McPherron, R. L., & Baker, D. N. (1985). Solar wind-magnetosphere energy input functions [Conference Proceedings]. In *Solar wind-magnetosphere energy input functions*.

Beharrell, M. J., & Honary, F. (2016). Decoding solar wind-magnetosphere coupling. *Space Weather*, *14*(10), 724–741. https://doi.org/10.1002/2016SW001467

Borovsky, J. E. (2021). Is our understanding of solar-wind/magnetosphere coupling satisfactory? *Frontiers in Astronomy and Space Sciences*, *8*. https://doi.org/10.3389/fspas.2021.634073

Borovsky, J. E., Thomsen, M. F., & Elphic, R. C. (1998). The driving of the plasma sheet by the solar wind. *Journal of Geophysical Research*, *103*(A8), 17617–17639. https://doi.org/10.1029/97JA02986

Burton, R. K., McPherron, R. L., & Russell, C. T. (1975). An empirical relationship between interplanetary conditions and Dst. *Journal of Geophysical Research (1896-1977)*, *80*(31), 4204–4214. https://doi.org/10.1029/JA080i031p04204

Cai, L., Ma, S. Y., & Zhou, Y. L. (2010). Prediction of SYM-H index during large storms by NARX neural network from IMF and solar wind data. *Annales Geophysicae*, *28*(2), 381–393. https://doi.org/10.5194/angeo-28-381-2010

Camporeale, E. (2019). The challenge of machine learning in space weather: Nowcasting and forecasting. *Space Weather-the International Journal of Research and Applications*, *17*(8), 1166–1207. https://doi.org/10.1029/2018sw002061

Collado-Villaverde, A., Muñoz, P., & Cid, C. (2021). Deep neural networks with convolutional and LSTM layers for SYM-H and ASY-H forecasting. *Space Weather-the International Journal of Research and Applications*, *19*(6). https://doi.org/10.1029/2021SW002748

Consolini, G. (2018). Chapter 7 - Emergence of dynamical complexity in the Earth's magnetosphere. In E. Camporeale, S. Wing, & J. R. Johnson (Eds.), *Machine learning techniques for space weather* (pp. 177–202). Elsevier. https://doi.org/10.1016/B978-0-12-811788-0.00007-X

Daglis, I. A. (2006). Ring current dynamics. *Space Science Reviews*, *124*(1–4), 183–202. https://doi.org/10.1007/s11214-006-9104-z

Daglis, I. A., Thorne, R. M., Baumjohann, W., & Orsini, S. (1999). The terrestrial ring current: Origin, formation, and decay. *Reviews of Geophysics*, *37*(4), 407–438. https://doi.org/10.1029/1999RG900009

Dai, L., Zhu, M. H., Ren, Y., Gonzalez, W., Wang, C., Sibeck, D., et al. (2024). Global-scale magnetosphere convection driven by dayside magnetic reconnection. *Nature Communications*, *15*(1), 639. https://doi.org/10.1038/s41467-024-44992-y

Dungey, J. W. (1961). Interplanetary magnetic field and the auroral zones. *Physical Review Letters*, *6*(2), 47–48. https://doi.org/10.1103/PhysRevLett.6.47

Ebihara, Y., & Ejiri, M. (2003). Numerical simulation of the ring current: Review. *Space Science Reviews*, *105*(1–2), 377–452. https://doi.org/10.1023/A:1023905607888

Finch, I., & Lockwood, M. (2007). Solar wind-magnetosphere coupling functions on timescales of 1 day to 1 year. *Annals of Geophysics*, *25*(2), 495–506. https://doi.org/10.5194/angeo-25-495-2007

Fok, M.-C., Kozyra, J. U., Nagy, A. F., & Cravens, T. E. (1991). Lifetime of ring current particles due to Coulomb collisions in the plasmasphere. *Journal of Geophysical Research*, *96*(A5), 7861–7867. https://doi.org/10.1029/90JA02620

Fok, M. C., Wolf, R. A., Spiro, R. W., & Moore, T. E. (2001). Comprehensive computational model of Earth's ring current. *Journal of Geophysical Research*, *106*(A5), 8417–8424. https://doi.org/10.1029/2000ja000235

Forsyth, C., Watt, C. E. J., Mooney, M. K., Rae, I. J., Walton, S. D., & Horne, R. B. (2020). Forecasting GOES 15>2 MeV electron fluxes from solar wind data and geomagnetic indices. *Space Weather-the International Journal of Research and Applications*, *18*(8). https://doi.org/10.1029/2019SW002416

Fu, H., Yue, C., Zong, Q.-G., Zhou, X., Yu, Y., Li, Y., et al. (2023). Substorm influences on plasma pressure and current densities inside the geosynchronous orbit. *Journal of Geophysical Research: Space Physics*, *128*(3), e2022JA031099. https://doi.org/10.1029/2022JA031099

Fu, S. Y., Zong, Q. G., Wilken, B., & Pu, Z. Y. (2001). Temporal and spatial variation of the ion composition in the ring current. *Space Science Reviews*, *95*(1–2), 539–554. https://doi.org/10.1023/A:1005212906199

Ganushkina, N., Jaynes, A., & Liemohn, M. (2017). Space weather effects produced by the ring current particles. *Space Science Reviews*, *212*(3–4), 1315–1344. https://doi.org/10.1007/s11214-017-0412-2

Gonzalez, W. D. (1990). A unified view of solar wind-magnetosphere coupling functions. *Planetary and Space Science*, *38*(5), 627–632. https://doi.org/10.1016/0032-0633(90)90068-2

Graham, D. B., Khotyaintsev, Y. V., André, M., Vaivads, A., Divin, A., Drake, J. F., et al. (2022). Direct observations of anomalous resistivity and diffusion in collisionless plasma. *Nature Communications*, *13*(1), 2954. https://doi.org/10.1038/s41467-022-30561-8

Hasegawa, H., Fujimoto, M., Phan, T. D., Rème, H., Balogh, A., Dunlop, M. W., et al. (2004). Transport of solar wind into Earth's magnetosphere through rolled-up Kelvin-Helmholtz vortices. *Nature*, *430*(7001), 755–758. https://doi.org/10.1038/nature02799

Iong, D., Chen, Y., Toth, G., Zou, S. S., Pulkkinen, T., Ren, J. E., et al. (2022). New findings from explainable SYM-H forecasting using gradient boosting machines. *Space Weather-the International Journal of Research and Applications*, *20*(8). https://doi.org/10.1029/2021SW002928

Jang, E., Yue, C., Zong, Q., Fu, S., & Fu, H. (2021). The effect of non-storm time substorms on the ring current dynamics. *Earth and Planetary Physics*, *5*(3), 251–258. https://doi.org/10.26464/epp2021032

Ji, Y., Ma, L., Shen, C., Zeng, G., Yang, Y. Y., & Ti, S. (2023). Composite model for predicting SYM-H index. *Earth and Space Science*, *10*(10). https://doi.org/10.1029/2022EA002560

Jordanova, V. K., Ilie, R., & Chen, M. W. (2020). Chapter 1 - Introduction and historical background. In V. K. Jordanova, R. Ilie, & M. W. Chen (Eds.), *Ring current investigations* (pp. 1–13). Elsevier. https://doi.org/10.1016/B978-0-12-815571-4.00001-9

Klimas, A. J., Vassiliadis, D., & Baker, D. N. (1997). Data-derived analogues of the magnetospheric dynamics. *Journal of Geophysical Research*, *102*(A12), 26993–27009. https://doi.org/10.1029/97JA02414

Li, T. K., Li, W. Y., Tang, B. B., Khotyaintsev, Y. V., Graham, D. B., Ardakani, A., et al. (2023). Kelvin-Helmholtz waves and magnetic reconnection at the Earth's magnetopause under southward interplanetary magnetic field. *Geophysical Research Letters*, *50*(20). https://doi.org/10.1029/2023GL105539

Lockwood, M. (2022). Solar wind-magnetosphere coupling functions: Pitfalls, limitations, and applications. *Space Weather-the International Journal of Research and Applications*, *20*(2). https://doi.org/10.1029/2021SW002989

Maggiolo, R., Hamrin, M., De Keyser, J., Pitkänen, T., Cessateur, G., Gunell, H., & Maes, L. (2017). The delayed time response of geomagnetic activity to the solar wind. *Journal of Geophysical Research: Space Physics*, *122*(11), 11109–11127. https://doi.org/10.1002/2016JA023793

Mayaud, P. N. (1980). What is a geomagnetic index? In *Derivation, meaning, and use of geomagnetic indices* (pp. 2–4). https://doi.org/10.1002/9781118663837.ch2

McPherron, R. L., & O'Brien, P. (2001). Predicting geomagnetic activity: The index. *Space Weather*, *125*, 339–345.

Nitta, N. V., Mulligan, T., Kilpua, E. K. J., Lynch, B. J., Mierla, M., O'Kane, J., et al. (2021). Understanding the origins of problem geomagnetic storms associated with "stealth" coronal mass ejections. *Space Science Reviews*, *217*(8), 82. https://doi.org/10.1007/s11214-021-00857-0

Pallocchia, G., Amata, E., Consolini, G., Marcucci, M. F., & Bertello, I. (2006). Geomagnetic index forecast based on IMF data only. *Annales Geophysicae*, *24*(3), 989–999. https://doi.org/10.5194/angeo-24-989-2006

Palmroth, M., Janhunen, P., & Pulkkinen, T. I. (2006). Hysteresis in solar wind power input to the magnetosphere. *Geophysical Research Letters*, *33*(3). https://doi.org/10.1029/2005GL025188

Perreault, P., & Akasofu, S. I. (1978). A study of geomagnetic storms. *Geophysical Journal International*, *54*(3), 547–573. https://doi.org/10.1111/j.1365-246X.1978.tb05494.x

Perreault, P. D. (1974). On the relationship between interplanetary magnetic fields and magnetospheric storms and substorms (Thesis). Retrieved from https://ui.adsabs.harvard.edu/abs/1974PhDT……10P

Pirjola, R., Kauristie, K., Lappalainen, H., Viljanen, A., & Pulkkinen, A. (2005). Space weather risk. *Space Weather-the International Journal of Research and Applications*, *3*(2). https://doi.org/10.1029/2004sw000112

Sandhu, J. K., Rae, I. J., Freeman, M. P., Forsyth, C., Gkioulidou, M., Reeves, G. D., et al. (2018). Energization of the ring current by substorms. *Journal of Geophysical Research: Space Physics*, *123*(10), 8131–8148. https://doi.org/10.1029/2018JA025766

Shen, C., Liu, Z. X., & Kamei, T. (2002). A physics-based study of the Dst-AL relationship. *Journal of Geophysical Research*, *107*(A1). https://doi.org/10.1029/2001ja900121

Siciliano, F., Consolini, G., Tozzi, R., Gentili, M., Giannattasio, F., & De Michelis, P. (2021). Forecasting SYM-H index: A comparison between long short-term memory and convolutional neural networks. *Space Weather-the International Journal of Research and Applications*, *19*(2). https://doi.org/10.1029/2020SW002589

Treumann, R. A., LaBelle, J., & Pottelette, R. (1991). Plasma diffusion at the magnetopause: The case of lower hybrid drift waves. *Journal of Geophysical Research*, *96*(A9), 16009–16013. https://doi.org/10.1029/91JA01671

Vasyliunas, V. M., Kan, J. R., Siscoe, G. L., & Akasofu, S. I. (1982). Scaling relations governing magnetospheric energy transfer. *Planetary and Space Science*, *30*(4), 359–365. https://doi.org/10.1016/0032-0633(82)90041-1

Wang, C., Han, J. P., Li, H., Peng, Z., & Richardson, J. D. (2014). Solar wind-magnetosphere energy coupling function fitting: Results froma global MHD simulation. *Journal of Geophysical Research-Space Physics*, *119*(8), 6199–6212. https://doi.org/10.1002/2014ja019834

Wanliss, J. A., & Showalter, K. M. (2006). High-resolution global storm index:: Versus SYM-H. *Journal of Geophysical Research: Space Physics*, *111*(A2). https://doi.org/10.1029/2005ja011034

Wing, S., Turner, D. L., Ukhorskiy, A. Y., Johnson, J. R., Sotirelis, T., Nikoukar, R., & Romeo, G. (2022). Modeling radiation belt electrons with information theory informed neural networks. *Space Weather-the International Journal of Research and Applications*, *20*(8). https://doi.org/10.1029/2022SW003090

Wu, J.-G., & Lundstedt, H. (1997). Neural network modeling of solar wind-magnetosphere interaction. *Journal of Geophysical Research*, *102*(A7), 14457–14466. https://doi.org/10.1029/97JA01081

Yu, Y., Ma, L., Wei, Z., An, D., Wu, H., Lu, H., & Cao, J. (2024). A storm-time ring current model (STRIM). *Science China Technological Sciences*, *67*(12), 3890–3908. https://doi.org/10.1007/s11431-024-2654-5

Yu, Y. Q., Cao, J. B., Pu, Z. Y., Jordanova, V. K., & Ridley, A. (2022). Meso-scale electrodynamic coupling of the Earth magnetosphere-ionosphere system. *Space Science Reviews*, *218*(8), 74. https://doi.org/10.1007/s11214-022-00940-0

Yue, C., Bortnik, J., Li, W., Ma, Q., Wang, C.-P., Thorne, R. M., et al. (2019). Oxygen ion dynamics in the Earth's ring current: Van Allen probes observations. *Journal of Geophysical Research: Space Physics*, *124*(10), 7786–7798. https://doi.org/10.1029/2019JA026801

Zhang, Q. H., Lockwood, M., Foster, J. C., Zhang, S. R., Zhang, B. C., McCrea, I. W., et al. (2015). Direct observations of the full dungey convection cycle in the polar ionosphere for southward interplanetary magnetic field conditions. *Journal of Geophysical Research-Space Physics*, *120*(6), 4519–4530. https://doi.org/10.1002/2015ja021172

Zhao, M. X., Le, G. M., & Lu, J. Y. (2022). Can we estimate the intensities of great geomagnetic storms (SYM-H -200 nt) with the burton equation or the O'Brien and mcpherron equation? *The Astrophysical Journal*, *928*(1), 18. https://doi.org/10.3847/1538-4357/ac50a8

Zhu, D., Billings, S. A., Balikhin, M., Wing, S., & Coca, D. (2006). Data derived continuous time model for the dynamics. *Geophysical Research Letters*, *33*(4). https://doi.org/10.1029/2005gl025022